The Astrophysical Journal, 908:72 (9pp), 2021 February 10 https://doi.org/10.3847/1538-4357/abcf29
© 2021. The American Astronomical Society. All rights reserved.

The Formation of Electron Outflow Jets with Power-law Energy Distribution in Guide-field Magnetic Reconnection

H. Che[1,2], G. P. Zank[1,2], A. O. Benz[3,4], B. Tang[1,2], and C. Crawford[1,2]
[1] Center for Space Plasma and Aeronomic Research (CSPAR), University of Alabama in Huntsville, Huntsville, AL 35805, USA; hc0043@uah.edu
[2] Department of Space Science, University of Alabama in Huntsville, Huntsville, AL 35899, USA
[3] University of Applied Sciences and Arts Northwestern Switzerland, CH-5210 Windisch, Switzerland
[4] Institute for Particle Physics and Astrophysics, ETH Zürich, 8093, Zürich, Switzerland
Received 2020 September 4; revised 2020 November 22; accepted 2020 November 29; published 2021 February 15

Abstract

Observationally, electron beams with power-law energy spectra are commonly associated with solar flares. Previous studies have found that during magnetic reconnection with a guide field B_g larger than 0.1 times the asymptotic field B_0, electron beams are unable to develop due to the strong deflection caused by the guide field. Using particle-in-cell simulations we show that in force-free reconnection, the development of an electron Kelvin–Helmholz instability can suppress the Hall effect and produce a flute-like outflow exhaust, in which both electrons and ions are nearly frozen-in with the magnetic field. The coupling of a continuously growing electron velocity shear and $\boldsymbol{E} \times \boldsymbol{B}$ drift drive the electrons out of magnetic vortices and results in collimated jets with a power-law energy spectrum in the elongated exhaust. The spatial density of electron jets is comparable to the background and is highly inhomogeneous, signifying on asymmetric density structure in guide field reconnection.

Unified Astronomy Thesaurus concepts: Solar magnetic reconnection (1504); Solar energetic particles (1491)

1. Introduction

Solar flares are intense impulsive events of radiation associated with the sudden release of magnetic energy stored in the magnetic loops associated with sunspots. As magnetic energy is released, particles, including both electrons and ions, are heated and accelerated in the solar corona. Observations show that a significant fraction of the released magnetic energy is converted into the kinetic energy of nonthermal energetic particles and plasma bulk motion (Sheeley et al. 2004; Qiu et al. 2004; Dennis et al. 2011; Zharkova et al. 2011; Vilmer 2012; Benz 2017). The energetic electrons produce radiation at all wavelengths from decameter radio waves to gamma rays. X-ray observations of the Sun and in situ observations in the vicinity of the Earth discovered that an inverse power-law energy distribution $f(W) \propto W^{-\alpha}$ (W is the particle kinetic energy, α is the energy spectral index) is a ubiquitous property of energetic particles from the Sun (Krucker et al. 2009; Lin 2011; Holman et al. 2011; Zharkova et al. 2011; Benz 2017). In addition, the association of Type III radio bursts with solar flares indicates that electron beams are generated in flares and are prevalent in the corona (Benz et al. 1992; White et al. 2011; Fletcher et al. 2011; Dennis et al. 2011; Reid & Ratcliffe 2014; Benz 2017). Simultaneous observations of fast solar wind electrons and Type III radio bursts show that similar to nonthermal energetic electrons in solar flares, the energy spectra of beam electrons can also be described with an inverse power law (Lin et al. 1973; Krucker et al. 2007), implying that the electron beams may have been transported directly out of the acceleration regions in solar flares.

Electron beams are an essential element of particle acceleration processes in solar flares. Electron beams produce coherent plasma emission via a nonlinear electron two-stream instability, manifested as Type III radio bursts whose frequency follows the local electron plasma frequency ω_{pe} or the harmonic as the electron beams move along magnetic field lines away from the acceleration region in the corona (Krucker et al. 2007; Reid & Ratcliffe 2014; Che et al. 2017). Radio bursts are hence a powerful observational tool to probe the plasma environment and dynamics in the acceleration region of solar flares (Benz et al. 1992; Dennis et al. 2011; Fletcher et al. 2011; White et al. 2011; Benz 2017; Kontar et al. 2017). Thanks to the recent launch of the Parker Solar Probe, Solar Orbiter, and other new high resolution ground-based radio and optical telescopes, such as DKIST, simultaneous high resolution observations of radio bursts, X-ray emission, and in situ detection of energetic particle are becoming possible. The understanding of electron beam formation and its connection to the origin of nonthermal energetic electrons is becoming increasingly important to obtain a complete picture of energetic particle production in solar flares. In addition, recent studies of solar wind have found that electron beams associated with nanoflares may be responsible for the origin of nonthermal electrons in the solar wind (Che & Goldstein 2014; Macneil et al. 2017; Che 2018; Che et al. 2019), making the study of the electron beams in the corona even more important.

Magnetic reconnection (MR) is found to play an essential role in charged particle energization in solar flares (e.g., Forbes & Priest 1984; Aschwanden 2002; Liu et al. 2008; Krucker et al. 2010; Zharkova et al. 2011; Benz 2017). Observations find clear associations between electron beams and reconnection acceleration regions where nonthermal energetic electrons and electron jets emerge (Krucker et al. 2010; Chen et al. 2018; Cairns et al. 2018). Particle acceleration in MR has been extensively investigated in the past (Pritchett & Wu 1979; Kliem 1994; Miller 1997; Drake et al. 2006; Medvedev & Zakutnyaya 2009; Petrosian 2012; Nishizuka & Shibata 2013; Zank et al. 2014; Klein & Dalla 2017), but how MR accelerates particles to an inverse power-law energy spectrum has remained unsolved. Models of reconnection acceleration fall into two categories: stochastic turbulence acceleration (Petrosian 2012) and acceleration by randomly distributed multi-islands. In the former case, it is found that to generate a power-

law spectrum by turbulent acceleration in the desired timescale is a challenge, or in other words, the origin of the desired turbulence is unclear and remains as a model assumption (Miller et al. 1996; Grigis & Benz 2006). PIC simulations show that instability-driven turbulence usually generates non-power-law plasma heating (Che et al. 2010; Daughton et al. 2011; Che et al. 2011; Dahlin et al. 2016; Lapenta et al. 2018; Muñoz & Büchner 2018) and thus how one generates the theoretically expected or desired turbulence in MR is a nontrivial question yet to be answered. In the latter case, the widely invoked scenario is acceleration in multi-islands driven by tearing instability (Drake et al. 2006; Daughton et al. 2011; Lin 2011). The problem with this scenario is that adiabatic acceleration via the contracting magnetic island is inefficient and the long trapping of particles in the islands leads to insufficient stochastic scattering, resulting in the failure to generate the power-law particle energy spectra for solar energetic electrons (Che & Zank 2019).

Guide field is very common in the solar corona MR compared to antiparallel MR most of the aforementioned models concern. The role of guide field in MR, however, is somewhat puzzling. Simulations find that a guide field can reduce the MR rate, and the outflow velocity is much lower than the asymptotic Alfvén velocity v_{A0} (Huba 2005). Further it was suggested that electron jets cannot form in MR with a guide field B_g larger than one-tenth of the asymptotic magnetic field B_0, due to the deflection by the guide field in the exhaust where electrons are demagnetized and decoupled from ions (Goldman et al. 2011) (see Section 2).

Recently Che & Zank (2020) showed that electrons can be efficiently accelerated to an inverse power-law energy distribution by an electron Kelvin–Helmholtz instability (EKHI) in force-free MR, a type of guide field MR that is common in the corona. The EKHI generates stochastic electric fields as the magnetic vortices expand quickly and the magnetic energy is inversely transferred from small to large scales. The random inductive electric fields accelerate electrons via a second-order Fermi-acceleration process, and the power-law index of the electron energy distribution is found to be determined by the guide field and the spatial scales of the vortices and inductive electric fields. The electron energy spectra show a two-stage soft–hard–harder evolution reflecting the linear–nonlinear stage in the evolution of the magnetic turbulence, qualitatively consistent with the observed two-stage, soft–hard–harder evolution of electron power spectra in the flares (Dennis 1988; Grigis & Benz 2008; Grayson et al. 2009; Gou et al. 2017).

In this paper, we show EKHI can also produce electron jets with a power-law energy spectrum in force-free guide field MR. With Particle-in-Cell (PIC) simulations, we demonstrate that electron jets with density similar to that of the background, and bulk velocity $\sim V_{A0} \sim 0.05c$ are produced together with the ion jets in the outflow exhaust of the MR. EKHI fully suppresses the Hall effect and forms a Sweet–Parker-like rather than a Petschek-like outflow exhaust. In the exhaust, electrons and ions are almost entirely coupled and frozen-in with the magnetic field. The electron and ion jets develop due to the continuous growth of the velocity shear, which in turn generates an electric field. The frozen-in condition leads the accelerated electrons to flow out of the magnetic vortices to form a collimated jet in the flute-like exhaust. Consequently, the electron jets share a similar power-law energy spectrum to the nonthermal energetic electrons in the magnetic vortices. Moreover, the spatial density distribution of electron jets is inherited from the asymmetric density structure in guide field MR.

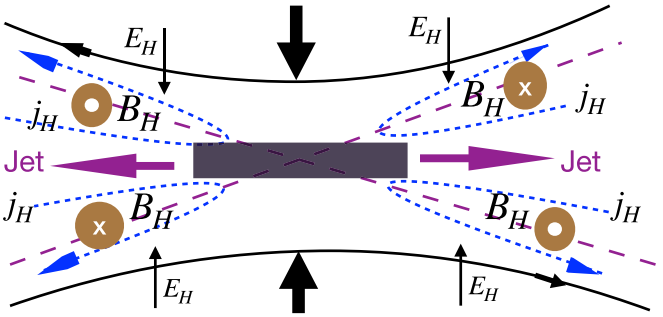

Figure 1. An illustration of the Hall current j_H (blue short-dashed lines), out-of-plane Hall magnetic field B_H, and Hall electric field E_H.

2. Electron Jet Formation in Hall-effect-dominated Magnetic Reconnection and the Effects of Guide Magnetic Field

In this section, we briefly review jet formation in Hall effect-dominated MR, and how a guide field can deflect and destroy the electron jets.

It is well known that the MR Hall effect can create a Petschek-like outflow exhaust that is essential for fast reconnection in collisionless plasma through the generation of a quadrupole out-of-plane magnetic field (Sonnerup 1979; Uzdensky & Kulsrud 2006). The essence of Hall physics is contained in the generalized Ohm's law (Birn et al. 2001). In the ion dissipation region of collisionless MR, the generalized Ohm's law is reduced to

$$\boldsymbol{E} + \frac{1}{c}\boldsymbol{V} \times \boldsymbol{B} = \frac{1}{\mathrm{nec}}\boldsymbol{j} \times \boldsymbol{B}, \tag{1}$$

where $\boldsymbol{V}$ is the velocity of plasma flow and $\boldsymbol{j}$ is the current density, and the approximation $\boldsymbol{V}_i \approx \boldsymbol{V}$ is used (Huba 2003). The R.H.S. is called the Hall term.

In the ion dissipation region but outside the electron dissipation region, electrons are frozen-in with the magnetic field while ions become demagnetized, and in this region electrons are decoupled from ions. A quadrupole out-of-plane magnetic field naturally arises due to the electron current that flows along the magnetic field lines in and out of the inner reconnection region to maintain charge neutrality, resulting in a widening pedestal-like outflow exhaust (Sonnerup 1979; Uzdensky & Kulsrud 2006). In Figure 1, we show the basic picture of Hall current and Hall fields. The Hall electron current $\boldsymbol{j}_H$ is in the xy plane, and the Hall magnetic field is out of plane, i.e., $\boldsymbol{B}_H = B_H\hat{z} = (B_z - B_g)\hat{z}$. If $B_g = 0$, then $B_H = B_z$. The Hall current is related to the Hall magnetic field by Ampere's law $\nabla \times \boldsymbol{B}_H = 4\pi\boldsymbol{j}_H/c$. We can see that the reversal of the Hall current marks the magnetic separatrix. The Hall electric field is generated through

$$\boldsymbol{E}_H = -\boldsymbol{v}_H \times \boldsymbol{B}_z/c, \tag{2}$$

where $\boldsymbol{v}_H = \boldsymbol{j}_H/en_e$. This expression is consistent with electrons being frozen-in at the flank, or $\boldsymbol{v}_H \approx v_{\mathrm{ex}}$, $\boldsymbol{E}_H \approx E_y\hat{y}$, and $v_{\mathrm{ex}} = v_{E\times B}$. Here $v_{E\times B} = cE_yB_z/B^2$ is the $E \times B$ drift. At the center of the current sheet, electrons also

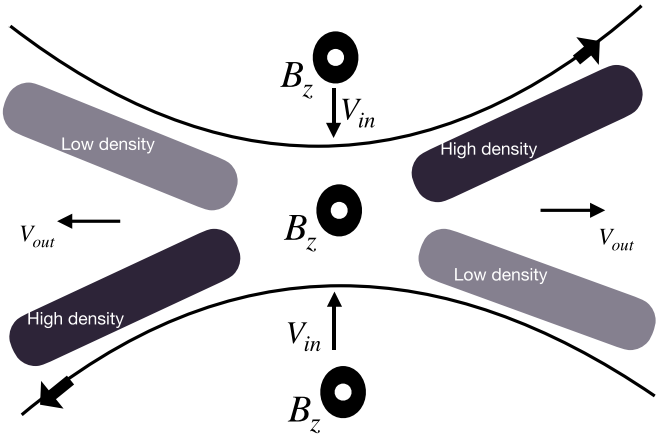

Figure 2. An illustration of the asymmetric density structure in guide-field magnetic reconnection.

become demagnetized and the electron frozen-in condition is broken too, resulting in $\boldsymbol{E} + \boldsymbol{v} \times \boldsymbol{B}/c \neq 0$. From the above picture we see that the Hall effect peaks at the flanks of the outflow exhaust and decreases to zero at the center of the current sheet (Drake et al. 2008; Goldman et al. 2016) where non-Hall effects dominate. Such effects include the non-gyrotropic pressure (Vasyliunas 1975; Hesse et al. 2008; Le et al. 2010), inertia, and anomalous turbulence effects (Che et al. 2011). We want to emphasize that while the above picture concerns the usual antiparallel MR, Hall effects play a similar role and generate a similar structure in force-free MR (Che et al. 2011) since the current sheet deviates from force-free balance once MR proceeds.

The presence of a guide magnetic field in MR distorts the quadrupole structure of the out-of-plane magnetic field but the Hall effects still play a role similar to that in antiparallel MR. However, a guide field changes the symmetric plasma density structure in antiparallel MR to an asymmetric density structure (Figure 2). A guide field reduces the gyro-radius of electrons and thus prevents the motion of electrons across the current layer, resulting in narrower current layers and a parallel electric field along the separatrix. Density cavities form as the electrons approach the separatrix and are accelerated toward the x-line by the parallel electric field (Birn & Priest 2007). We will see in the next section that this specific feature in guide field MR will be preserved in the highly inhomogenous density distribution of electron jets.

An outstanding problem arising in guide-field MR simulations is why a guide field stronger than 0.1 B_0 can prevent the development of electron outflow jets as seen in antiparallel MR simulations (Goldman et al. 2011). At the center of the outflow exhaust, the breaking of the electron frozen-in condition implies that the in-plane residues of $\boldsymbol{E} + \boldsymbol{v} \times \boldsymbol{B}/c$ can accelerate electrons in both x and y directions. In the $B_g = 0$ case, the residues lead to an oscillation of electrons in the y-direction and the electron trajectory is bounded in y while moving in the x-direction. When $B_g \neq 0$, the residues lead to growing as well as oscillating motion in the y-direction, the electron trajectories all become unbounded in y and leave the jet direction at a distance closer and closer to the X-point of MR as B_g increases. This problem is particularly important given that guide field MR is very common in the corona, as are electron beams.

For guide field MR to produce the observed electron beams, the MR process needs to be very different from that described so far in this section, and the beams produced should also be qualitatively different from the small demagnetized electron jets seen in antiparallel MR simulations.

3. Simulations and Results

In this section we present a case study of outflow jet formation in force-free guide field MR. The 2D space and 3D momentum PIC MR simulation using the *p3d* code (Zeiler et al. 2002) is conducted with double force-free current sheets and periodic boundary conditions. The simulation domain has dimensions $L_x \times L_y = 128d_i \times 32d_i$ with grid number 16384×4096. The particle number per cell is 100 for each species. The initial magnetic field is $B_x/B_0 = \tanh[(y - L_y/2)/w_0]$, where B_0 is the asymptotic amplitude of B_x, w_0 is the half-width of the initial current sheet. The guide field $B_g^2 = B^2 - B_x^2$ is chosen so that $|B|$ is constant and the guide field is in the z-direction, i.e., $B_g = B_z\hat{z}$. In our simulation, we have adopted $w_0 = 0.5d_i$, $B_g = 2.5B_0$ and $B^2 = 7.25B_0^2$, where $d_i \equiv c/\omega_{pi}$ and $\omega_{pi,0}$ is the initial ion plasma frequency. Initially the velocity distribution functions of electrons and ions are isotropic Maxwellians with temperatures $T_{e0} = T_{i0}$, and $\beta = 0.04$. The mass ratio is $m_i/m_e = 100$ and the ratio of the initial electron plasma frequency ω_{pe} to the initial asymptotic electron gyrofrequency is 2. In the simulation the temperature is normalized to $m_i v_{A0}^2$ ($v_{A0} = B_0/(4\pi n_0 m_i)^{1/2}$ is the asymptotic ion Alfvén wave speed), mass is normalized to m_i, density to the asymptotic density n_0, the magnetic field to B_0, and the electric field to $E_0 = v_{A0}B_0/c$. The velocity is normalized to v_{A0}. MR is initialized to produce a primary x-line at $x = L_x/4 = 32d_i$ and an island centered at $x = 3L_x/4 = 96d_i$ in the top half of the domain, the bottom half of the domain is identically initialized but with the primary x-line at $x = 3L_x/4 = 96d_i$ and the island at $x = L_x/4 = 32d_i$ instead. The total simulation time is $\Omega_i t = 60$, where $\Omega_i = eB_0/m_i c$ is the asymptotic ion gyrofrequency.

In Figures 3 and 4, we show j_{ez} and v_{ex} at different times to demonstrate the evolution of the EKHI and the MR. In the force-free current sheet, $\boldsymbol{j} \times \boldsymbol{B} = 0$ requires $j_{\rm ex} \neq 0$ and the velocity component v_{ex} to be antiparallel above and below the midplane of the current sheet. As MR proceeds, the current sheet j_{ez} shrinks, the velocity shear becomes stronger. Similar to a fluid Kelvin–Helmholtz instability, the antiparallel electron velocity shear triggers an EKHI. The growth rate of EKHI is proportional to the velocity shear of the electron fluid flow $\Delta v_{\rm ex}$ (Chandrasekhar 1961). EKHI starts to grow slowly around $\Omega_i t \sim 20$, when the x-line and the magnetic island also start to develop. At $\Omega_i t \sim 40$, the width of the current sheet j_{ez} reaches d_e and the velocity shear significantly exceeds the local electron Alfvén wave speed $v_{\rm Ae}$, and the fast increase of the velocity shear $\Delta v_{\rm ex}$ leads to a fast growing phase of the EKHI. A chain of vortices quickly forms around the x-line and the EKHI enters the nonlinear stage. At this stage the magnetic vortices expand and merge quickly, until the instability saturates. The expansion of the in-plane magnetic vortices generates out-of-plane stochastic inductive electric fields δE_z. The stochastic E_z efficiently accelerates electrons within magnetic vortices in the z-direction. Che & Zank (2020) show that the mean electron acceleration over one electron gyro-

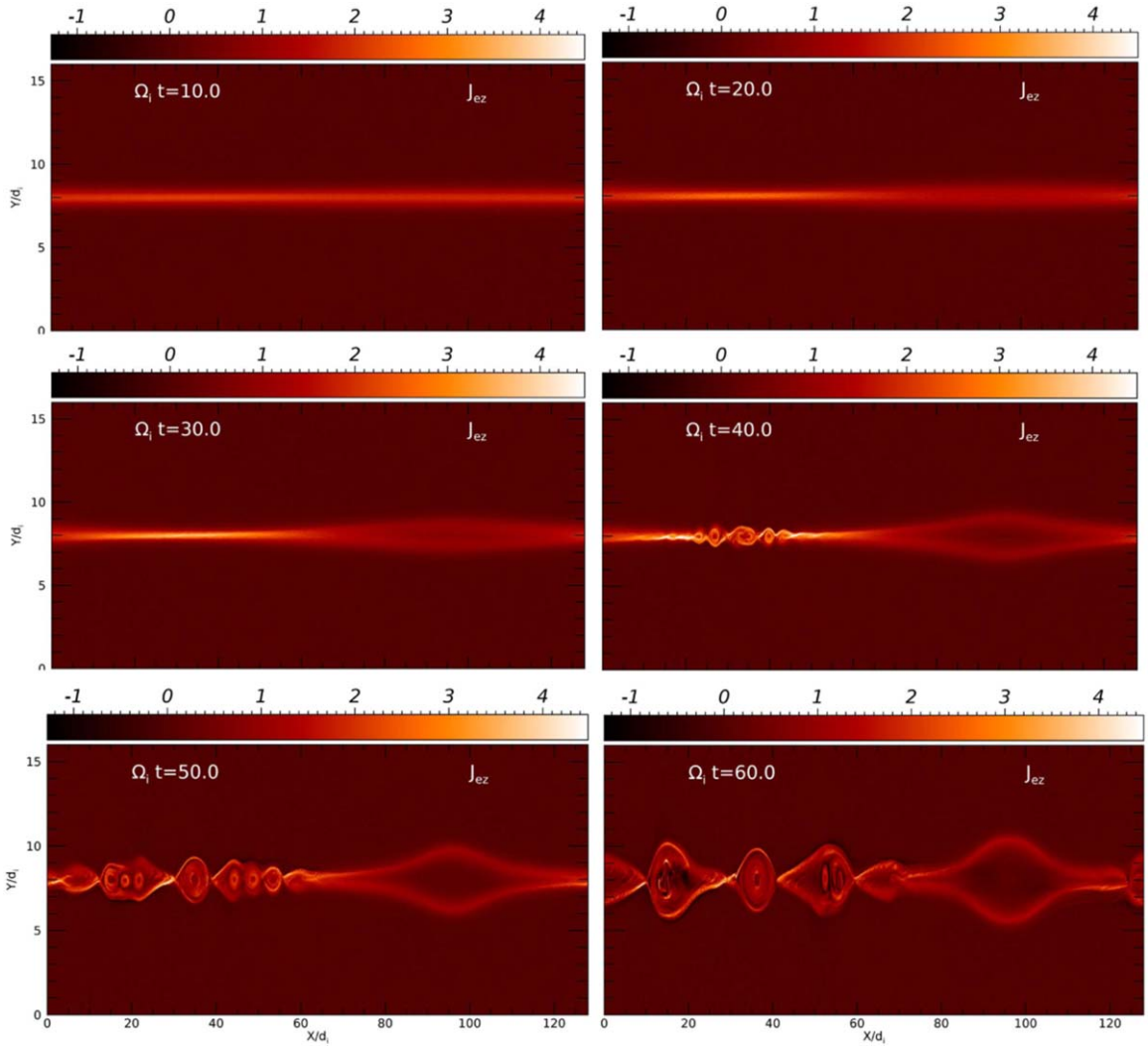

Figure 3. Time evolution of j_{ez}, a quantity that best illustrates the structure of the reconnection, in the top half of the simulation domain. Vortices, the x-line, and the reconnection island are shown.

period satisfies

$$\frac{\delta v_z}{\delta t} \sim \frac{1}{2}\frac{v_z}{\tau_g}\left(\frac{v_L}{c}\right)^2, \tag{3}$$

where v_L is the electron gyro-velocity, τ_g is the growth time of the EKHI, and $\tau_g \gg \Omega_e^{-1}$, and Ω_e is the electron gyrofrequency. In this equation the mean energy gain per gyro-period is $\propto (v_L/c)^2 \ll 1$, and thus this is a second-order Fermi acceleration (Fermi 1949).

Stochastic electric field acceleration in the magnetic vortices produces a power-law electron energy distribution, as shown in Figure 7. The slow and fast growth phases of the EKHI correspond to a two-phase soft–hard acceleration process, which is also reflected in the evolution of electron energy distributions. The electron energy spectrum $f(W) \propto W^{-\alpha}$ evolves from soft to hard as the index α decreases from 6 at $\Omega_i t = 20$ to the saturation value of 3.5 after $\Omega_i t = 40$. Che & Zank (2020) have shown that the steady power-law spectrum is determined by the ratio of the guide field B_g and the asymptotic magnetic field B_0, as well as the ratio of the spatial scales of inductive electric field D and that of the magnetic vortices R (Che & Zank 2020):

$$f(W) \propto W^{-(1+4a^2\frac{D}{R})/2}, \tag{4}$$

where $a \equiv B_g/B_0$. In this simulation, $a = 2.5$ and $D/R \sim 0.25$ when the EKHI saturates. The predicted spectral index $\alpha \sim 3.5$ is consistent with the simulation.

As the magnetic vortices grow and merge with each other on the left half of the domain where the primary x-line of the MR lies, the main body of the magnetic island on the right side becomes rounder. Collisions with magnetic vortices break the magnetic field lines at the two ends of the magnetic island. The EKHI driven secondary reconnections suppress the initial MR and reform the structure of the outflow exhaust. As a result the open-end exhaust (or Petschek-like exhaust) is replaced by a flute-like (or Sweet–Parker-like) exhaust as shown in Figures 4 and 5. At the same time, electron jets emerge from the vortices adjacent to the magnetic island and flow toward the center of the island. Around $\Omega_i t = 50$, when the system has entered the fast acceleration phase, we observe electron jets with a speed $\sim v_{A0}$ forming in the exhaust as shown in Figure 4.

In Figure 5, we can see more clearly the magnetic structure at the locations of the electron jets. The flute-like exhaust extends into the center of the adjacent magnetic vortices where

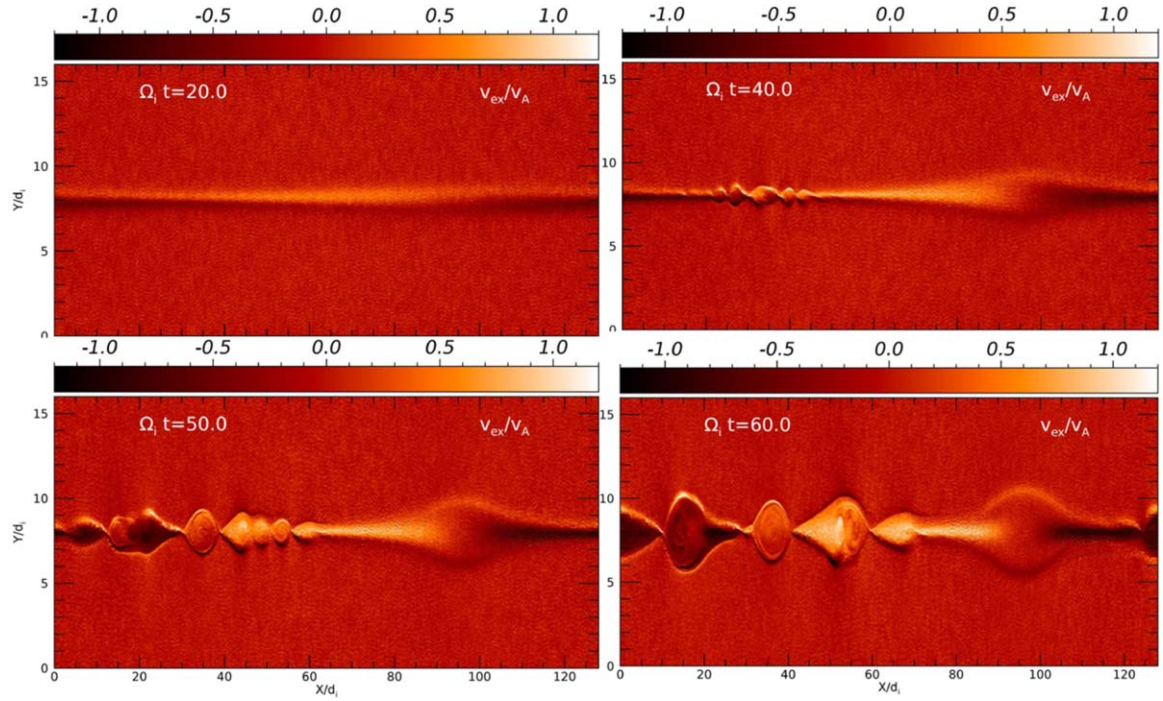

Figure 4. $v_{\rm ex}/v_{A0}$ in the top half of the domain at different times. Two opposing electron jets with speed $\sim v_{A0}$ develop near the x-line at the late-stage of the MR.

a local x-line is produced due to the merging of magnetic vortices. From the magnetic potential contour, we see that the strength of the magnetic field inside the magnetic vortices is much stronger than that inside the reconnection magnetic island. The whirlpools generated by the angular momentum of the electron flow cause the magnetic field lines to intertwine. As the vortices expand, the field energy is more efficiently dissipated and inversely transferred from small to large scales. On the other hand, the magnetic island releases magnetic energy through the contraction of the island, which is nearly incompressible and the area of the island is approximately conserved while the perimeter of the island becomes shorter. Since the timescale of the main MR is much longer than the growth time of EKHI, the magnetic energy dissipation in the magnetic island is much slower (Che & Zank 2019). The strengthened magnetic fields at the elongated exhaust confine the electron flow. As the electron jets originate from the vortices, the temperature is expected to be higher than that of the ambient. In Figure 5(b), the mean temperature of the electron jets is $T_e \sim 0.12 m_i v_{A0}^2$, which is about three times the ambient temperature. Another significant feature in Figure 5(c) is that the density of the jets is highly inhomogeneous in the y-direction: the density of the electron jets on the upper side is higher than that on the lower side, but the mean density of the electron jet is still close to that of the background—this feature can be traced back to the asymmetric density structure in guide field MR, and is preserved as the electrons move along the separatrix and become part of the electron outflow jet.

In Figure 5(d) we also show the ion jets with bulk speed $\sim v_{A0} \sim 0.05c$ that accompany the electron jets at the exhaust. To understand what drives both the electron and ion jets, we show the $\boldsymbol{E}\times\boldsymbol{B}/c$ drift (denoted as $\boldsymbol{v}_{E\times B}$) in Figure 5(e). Comparing Figures 5(a), (d), and (e), it is apparent that $\boldsymbol{v}_{E\times B}$ roughly matches the velocities of the electron and ion jets, which means both ions and electrons are magnetized in the elongated exhaust. In Figure 5(f), we further show the cuts along y at $x = 80d_i$ for v_{ex}, v_{ix}, $\boldsymbol{v}_{E\times B} = c\boldsymbol{E}\times\boldsymbol{B}/B^2$, and the components $-cE_zB_y/B^2$ and cE_yB_z/B^2 of $\boldsymbol{v}_{E\times B}$. A very small difference ($\sim 0.05 v_{A0}$) between v_{ex} and v_{ix} is observed and both are close to $\boldsymbol{v}_{E\times B}$. While close to each other, the value of $\boldsymbol{v}_{E\times B}$ is in between the velocities of the electron and ion jets, which means electron jets are slightly accelerated while ion jets are slightly decelerated by a very weak E_x, and both the jet ions and electrons are nearly magnetized. It is also clear that the dominant contribution to $\boldsymbol{v}_{E\times B}$ is from E_yB_z. The contribution from $-E_zB_y$ is close to zero due to the very small B_y along the jets, where the magnetic field lines are nearly parallel to the x-axis (see the magnetic field contour in Figure 5(a)).

The fact that the ions and electrons are frozen-in in the outflow exhaust in multivortices MR completely eliminates the traditional role of the Hall fields $\boldsymbol{B}_H = (B_z - B_g)\hat{z}$ and $\boldsymbol{E}_H = E_y\hat{y}$ in creating the pedestal-like outflow exhaust (see Section 2). In Hall effect-dominated reconnection, the Hall current and fields are peaked at the flank of the outflow jet and decrease to zero at the center of the current sheet. At the center of the current sheet where outflow jets form, electrons are demagnetized and $E_y\hat{y} + v_{\rm ex}\hat{x}\times B_z\hat{z}/c \neq 0$. In the presence of a guide field, the demagnetization results in a residue field that deflects the outflow electrons to the separatrix quickly and eventually diffuses the electron jets (see Section 1). In our multivortices MR with a guide field, the suppression of the Hall effect leads to an elongated exhaust and well-collimated outflow electron jets. The role of guide field B_z in this case changes to enhance the magnetization and the formation of electron outflow jets. We show the time evolution of B_z and E_y slices taken along the center of the current sheet in Figure 6. When the EKHI enters its fast growing stage, it is obvious that B_z around the x-line displays a wave-like structure that traces the magnetic vortices, but on the magnetic island side B_z almost does not change. On the other hand, the increasing of the electron velocity shear v_{ex} results in an increasing E_y in the region from $x \sim 40d_i$ to $x \sim 90d_i$ from where the electron jet

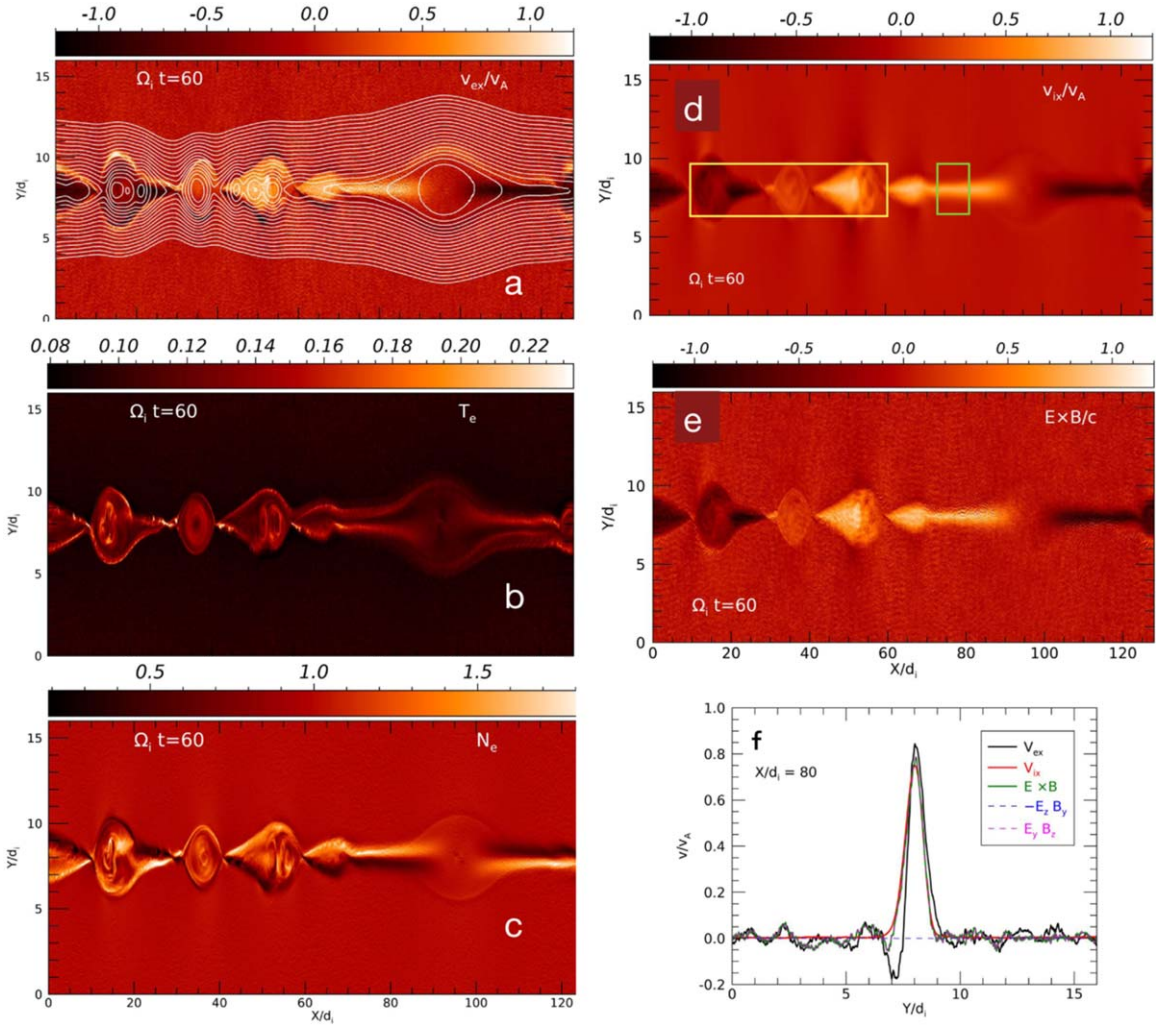

Figure 5. Quantities from the simulation at $\Omega_i t = 60$: (a) v_{ex} and the magnetic field shown as 2D magnetic potential contours; (b) the electron temperature; (c) electron density n_e; (d) ion velocity v_{ix}; (e) $\boldsymbol{v}_{E\times B}$ drift in the MR plane; (f) cuts of v_{ex}, v_{ix}, and drift $\boldsymbol{v}_{E\times B}$, as well as the components of the drift at $x/d_i = 80$. The velocity is normalized to v_{A0}. The small and large boxes in (d) are the regions where the electron energy spectra for jets (green) and vortices (yellow) shown in Figure 7 are taken, respectively.

originates (the negative E_y corresponds to the opposing electron jet produced by the other vortex next to the magnetic island). We also plot the spatial evolution of B_z and E_y in the y-direction inside the outflow exhaust at $x = 80d_i$. We see both B_z and E_y peak at the center of the current sheet, which is very different from Hall-dominated MRs. $B_z$and E_y also produce an ion outflow jet, and that explains why the spatial dimensions of the ion jets are similar to those of the electron jets.

We have shown that the electron jets in the outflow exhaust originate in the vortices driven by EKHI. In Figure 7 we show the electron energy distribution in one of the jets on the right side of the x-line (solid lines). Compared to the electron energy distribution in the vortices (dashed lines), a slight difference appears during the second nonlinear acceleration stage after $\Omega_i t = 30$, when the jet's power-law electron spectrum at the high energy end hardens gradually rather than jumps to the saturated stage. The reason is that the jet electrons are mixed with background electrons accelerated in the contracting island (Che & Zank 2020).

4. Discussion and Conclusions

In collisionless MR, the Hall effect plays a crucial role in facilitating fast reconnection. Simulations show that in Hall-effect-dominated MR outflow electron jets can form at the center of the MR exhaust. However, the results from Goldman et al. (2011, 2016) suggest that even with a very small guide field ($B_g/B_0 > 0.1$) the electron jets would be destroyed by deflection. This appears to be somewhat puzzling and even contradictory to observations that guide field MRs are common in the solar corona, and electron beams are commonly associated with coronal MR events.

In this paper, we investigate jet/beam formation in turbulent MR. Our case study concerns fast MR in a force-free current sheet in which a strong electron Kelvin–Helmholtz instability (EKHI) develops and the Hall-effect is suppressed. Our 2.5D PIC simulation has a large guide field $B_g = 2.5B_0$, and the simulation demonstrates for the first time that electron and ion jets can develop in strong guide field MR. In the simulation, strong EKHI are driven by the in-plane electron velocity shear. The EKHI experiences a slow and a fast growth phase, generates a chain of magnetic vortices whose expansion efficiently dissipates the magnetic energy. As found previously,

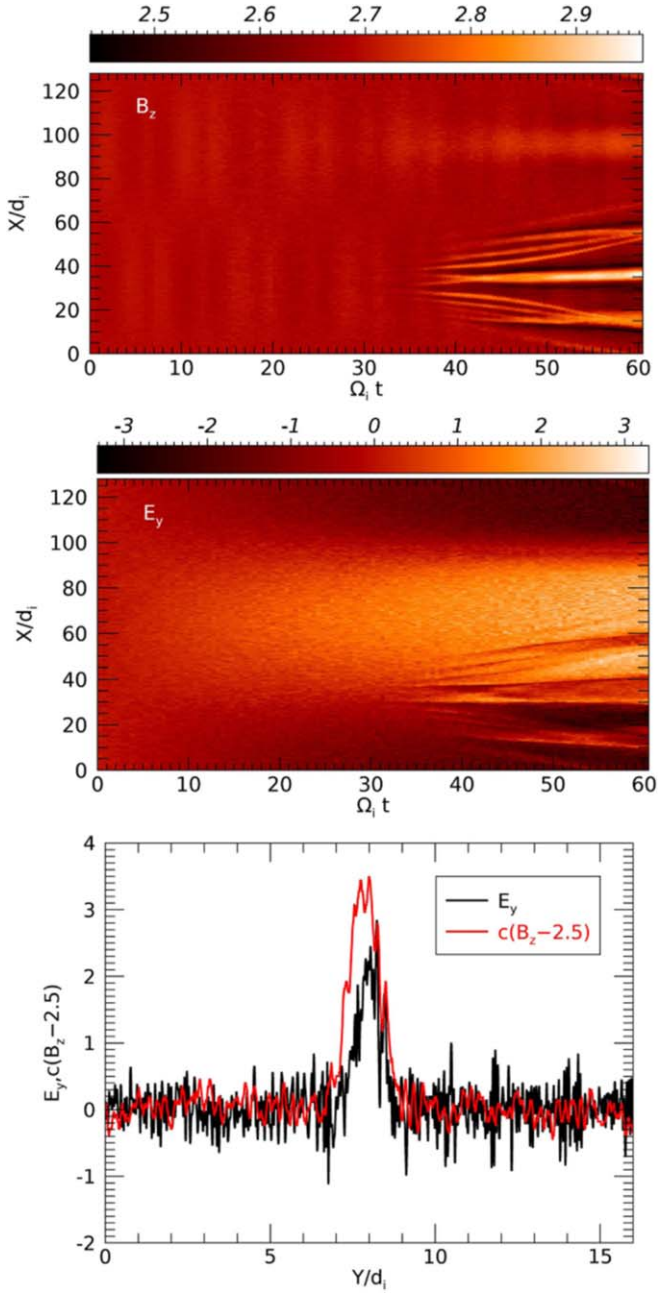

Figure 6. Top: the time stacks of cuts of B_z along x at $y = 8d_i$. Middle: the time stacks of cuts of E_y/E_0 along x at $y = 8d_i$. Bottom: E_y and B_z as a function of y at $x = 80d_i$ and $\Omega_i t = 60$.

the induced stochastic electric fields lead to a second-order Fermi-acceleration and produce a power-law electron energy spectrum that evolves from soft to hard through a two-stage acceleration process. The EKHI suppresses the Hall effect via the interaction between the magnetic vortices and the magnetic island, and reshapes the exhaust into a flute-like structure whose magnetic field is strongly enhanced by the increased tension of magnetic field lines. Both the jet electrons and ions are almost completely frozen-in with the magnetic field and are collimated within the elongated exhaust. Since the electron beams originate from magnetic vortices they have similar energy spectra, though the hardening of the energy spectrum in the jets is slower than that in vortices due to mixing with background electrons. On the other hand, the temperature of

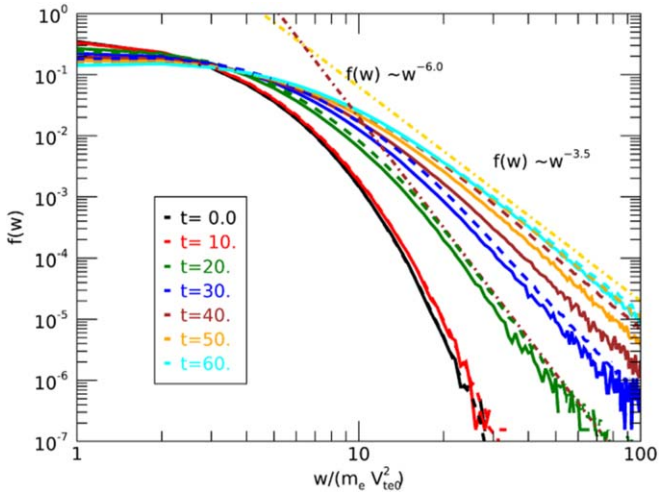

Figure 7. The electron energy spectrum at different evolution stages of EKHI in the electron jet at the outflow exhaust of the magnetic island near the x-line (solid lines) and in the magnetic vortices (dashed lines). For the regions for the electron energy spectra in jets and vortices, see Figure 5.

electron jets is much higher than the background due to plasma heating by EKHI, and the mean density of electron jets is close to that of the background but the density is highly inhomogeneous in the perpendicular direction, a feature that is inherited from the asymmetric density structure in guide-field MR.

In the past decade, the leading MR electron acceleration model is first-order Fermi acceleration from contracting magnetic islands generated by a tearing instability (Che & Zank 2019, and references therein). This model, however, suffers from a possible injection problem, as the mechanism cannot produce a power-law electron energy distribution if the MR is initially nonrelativistic. Since in our simulation, the jet electrons originate in the turbulent acceleration region in the EKHI vortices, and inherit the power-law energy spectra of energetic electrons. This is a unique character of the outflow jets in our model. Similar to the accelerated electrons in the magnetic vortices, the power-law electron energy spectra of the jets $f(W) \approx W^{-\alpha}$ evolve from soft to hard, i.e., from $\alpha \sim 6$ to $\alpha \sim 3.5$. Both the in situ and X-ray observations by Lin et al. (1973) and Krucker et al. (2007) suggest that beam electrons produced by solar flares have a high energy power-law spectral tail. We show the in situ observations of beam electrons at 1 AU and the X-rays beyond 47 keV in Figure 8. The simultaneous radio and X-ray observations confirm that the observed energetic electrons originate from the solar flare electron beams. The power-law spectral index of in situ energetic electrons is ∼3.9 and the high energy X-ray spectral index is ∼3.4. Both indices are close to the index of the power-law spectrum of the beam electrons in our simulation at saturation.

As discussed earlier, the index of electron energy spectrum at saturation is related to the guide field via Equation (4)

$$f(W) \propto W^{-(1+4a^2\frac{D}{R})/2}.$$

A stronger guide field may produce a larger index, and it depends on how the strength of magnetic field affects the development of the EKHI, especially how guide field affects the ratio of D/R, needs further investigation.

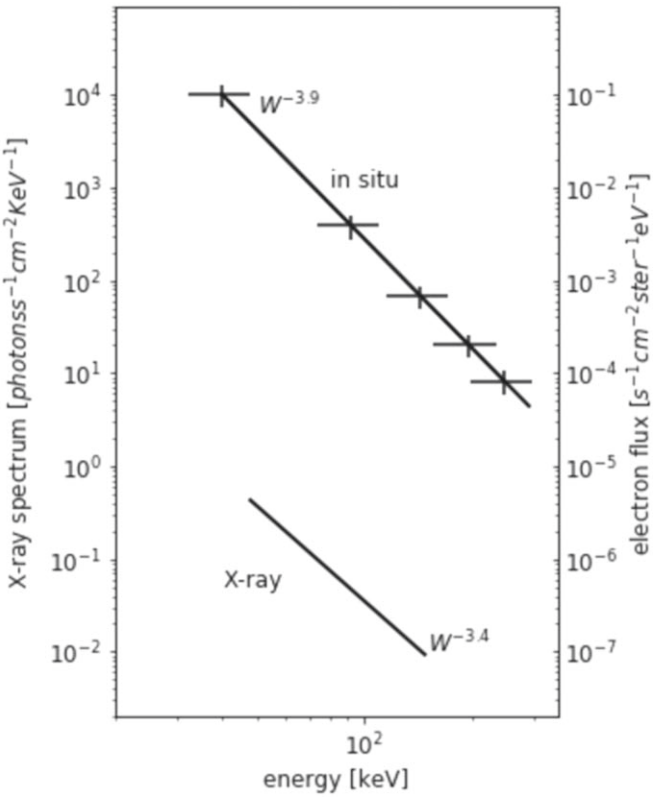

Figure 8. Observational spectra for energy beyond 47 keV for the event of 2002 April 14 cited from Figure 4 in the paper by Krucker et al. (2007). The top curve shows the in situ observed energetic electron peak flux spectrum. The bottom curve shows the observed X-ray spectrum.

Our simulations reveal that the bulk speed of the electron jets is about v_{A0}, which translates in solar flares as about $6000\,\mathrm{km\,s^{-1}} \sim 0.02\,c$. The temperature at the location of electron jets is higher than surrounding background electrons since the plasma experiences strong heating due to the EKHI. Thus it is very possible that in most cases electron jets cannot trigger a beam instability in the immediate vicinity of the reconnection site since the speed of the electron jets does not exceed the threshold for the electron two-stream instability, and hence do not produce Type III radio bursts (Che et al. 2017) near the acceleration region.

The non-Maxwellian energetic electrons in the jets may develop electron beams as they escape from the acceleration region of the MR. These electron beams may trigger the beam instabilities away from the acceleration region, where the ambient plasma temperature is lower than in the vicinity of the acceleration region, and the condition for beam instability is satisfied. The details of beam transport in the corona and beyond needs further investigation. At least this picture is qualitatively consistent with some observations of solar flares, in which the energetic electrons producing X-rays are found to be near the acceleration region while the electron beams producing Type III radio bursts are found at a distance away from the MR acceleration region (Cairns et al. 2018; Chen et al. 2018).

X-ray observations can provide useful information about the properties of the coronal electron jets. Krucker et al. (2010) argued that the large X-ray flux requires the density of electron jets to be comparable to the electron density of the background in the electron acceleration region. This result has presented a challenge, as no known mechanism can efficiently accelerate such a large number of electrons in just a few seconds. As we have seen in our simulations, high density, large index, and power-law distribution are the basic properties of electron jets produced by EKHI in MR. On the other hand, Chen et al. (2018) discovered that the density of electron jets is highly inhomogeneous in the acceleration region and this is also consistent with our simulation results.

In this paper, we have demonstrated that EKHI can naturally occur in force-free MR. However, the formation of electron jets depends on whether the magnetic vortices can suppress the Hall effect in MR and enable the formation of flute-like outflow exhausts. This does not always happen. For example, In the previous simulation by Che & Zank (2020), the interaction of magnetic vortices with magnetic island is weak and does not sufficiently suppress the Hall-effect. Consequently, there are no electron jets developed in the outflow region, and the energy spectrum of the electrons confined in the magnetic island is nonthermal but not a power law. Under what conditions electron jets with a power-law energy spectrum can form needs further study.

H.C. is very grateful to Dr. Y. Yang for his help in analyzing the simulations and providing critical comments on the manuscript. H.C., B.T., and C.C. acknowledge partial support of NASA Heliophysics Career award No. 80NSSC19K1106 and ORAU Ralph E. Powe Junior Faculty Enhancement Awards. H.C. and G.P.Z. acknowledge the partial support of an NSF EPSCoR RII-Track-1 Cooperative Agreement OIA-1655280. G.P.Z. acknowledges partial support from an NSF/DOE Partnership in Basic Plasma Science and Engineering via NSF grant PHY-1707247. The simulations were supported by the NASA High-End Computing (HEC) Program through the NASA Advanced Supercomputing (NAS) Division at Ames Research Center.

ORCID iDs

H. Che https://orcid.org/0000-0002-2240-6728
G. P. Zank https://orcid.org/0000-0002-4642-6192
A. O. Benz https://orcid.org/0000-0001-9777-9177

References

Aschwanden, M. J. 2002, SSRv, 101, 1
Benz, A. O. 2017, LRSP, 14, 2
Benz, A. O., Magun, A., Stehling, W., & Su, H. 1992, SoPh, 141, 335
Birn, J., Drake, J. F., Shay, M. A., et al. 2001, JGR, 106, 3715
Birn, J., & Priest, E. R. 2007, in Reconnection of Magnetic Fields: Magnetohydrodynamics and Collisionless Theory and Observations, ed. J. Birn & E. R. Priest (Cambridge: Cambridge Univ. Press), 2007
Cairns, I. H., Lobzin, V. V., Donea, A., et al. 2018, NatSR, 8, 1676
Chandrasekhar, S. 1961, Hydrodynamic and hydromagnetic stability (Oxford: Clarendon)
Che, H. 2018, JPhCS, 1100, 012005
Che, H., Drake, J. F., & Swisdak, M. 2011, Natur, 474, 184
Che, H., Drake, J. F., Swisdak, M., & Yoon, P. H. 2010, GeoRL, 37, 11105
Che, H., & Goldstein, M. L. 2014, ApJL, 795, L38
Che, H., Goldstein, M. L., Diamond, P. H., & Sagdeev, R. Z. 2017, PNAS, 114, 1502
Che, H., Goldstein, M. L., Salem, C. S., & Viñas, A. F. 2019, ApJ, 883, 151
Che, H., & Zank, G. P. 2019, JPhCS, 1332, 012003
Che, H., & Zank, G. P. 2020, ApJ, 889, 11
Chen, B., Yu, S., Battaglia, M., et al. 2018, ApJ, 866, 62
Dahlin, J. T., Drake, J. F., & Swisdak, M. 2016, PhPl, 23, 120704
Daughton, W., Roytershteyn, V., Karimabadi, H., et al. 2011, NatPh, 7, 539
Dennis, B. R. 1988, SoPh, 118, 49

Dennis, B. R., Emslie, A. G., & Hudson, H. S. 2011, SSRv, 159, 3
Drake, J. F., Shay, M. A., & Swisdak, M. 2008, PhPl, 15, 042306
Drake, J. F., Swisdak, M., Che, H., & Shay, M. A. 2006, Natur, 443, 553
Fermi, E. 1949, PhRv, 75, 1169
Fletcher, L., Dennis, B. R., Hudson, H. S., et al. 2011, SSRv, 159, 19
Forbes, T. G., & Priest, E. R. 1984, SoPh, 94, 315
Goldman, M. V., Lapenta, G., Newman, D. L., Markidis, S., & Che, H. 2011, PhRvL, 107, 135001
Goldman, M. V., Newman, D. L., & Lapenta, G. 2016, SSRv, 199, 651
Gou, T., Veronig, A. M., Dickson, E. C., Hernand ez-Perez, A., & Liu, R. 2017, ApJL, 845, L1
Grayson, J. A., Krucker, S., & Lin, R. P. 2009, ApJ, 707, 1588
Grigis, P. C., & Benz, A. O. 2006, A&A, 458, 641
Grigis, P. C., & Benz, A. O. 2008, ApJ, 683, 1180
Hesse, M., Zenitani, S., & Klimas, A. 2008, PhPl, 15, 112102
Holman, G. D., Aschwanden, M. J., Aurass, H., et al. 2011, SSRv, 159, 107
Huba, J. D. 2003, in Hall Magnetohydrodynamics—A Tutorial, ed. J. Büchner, C. Dum, & M. Scholer, Vol. 615 (Berlin: Springer), 166
Huba, J. D. 2005, PhPl, 12, 012322
Klein, K.-L., & Dalla, S. 2017, SSRv, 212, 1107
Kliem, B. 1994, ApJS, 90, 719
Kontar, E. P., Yu, S., Kuznetsov, A. A., et al. 2017, NatCo, 8, 1515
Krucker, S., Hudson, H. S., Glesener, L., et al. 2010, ApJ, 714, 1108
Krucker, S., Kontar, E. P., Christe, S., & Lin, R. P. 2007, ApJL, 663, L109
Krucker, S., Oakley, P. H., & Lin, R. P. 2009, ApJ, 691, 806
Lapenta, G., Pucci, F., Olshevsky, V., et al. 2018, JPlPh, 84, 715840103
Le, A., Egedal, J., Daughton, W., et al. 2010, GeoRL, 37, L03106
Lin, R. P. 2011, SSRv, 159, 421
Lin, R. P., Evans, L. G., & Fainberg, J. 1973, ApJL, 14, 191
Liu, W., Petrosian, V., Dennis, B. R., & Jiang, Y. W. 2008, ApJ, 676, 704
Macneil, A. R., Owen, C. J., & Wicks, R. T. 2017, AnGeo, 35, 1275
Medvedev, M. V., & Zakutnyaya, O. V. 2009, ApJ, 696, 2269
Miller, J. A. 1997, ApJ, 491, 939
Miller, J. A., Larosa, T. N., & Moore, R. L. 1996, ApJ, 461, 445
Muñoz, P. A., & Büchner, J. 2018, ApJ, 864, 92
Nishizuka, N., & Shibata, K. 2013, PhRvL, 110, 051101
Petrosian, V. 2012, SSRv, 173, 535
Pritchett, P. L., & Wu, C. C. 1979, PhFl, 22, 2140
Qiu, J., Lee, J., & Gary, D. E. 2004, ApJ, 603, 335
Reid, H. A. S., & Ratcliffe, H. 2014, RAA, 14, 773
Sheeley, N. R. J., Warren, H. P., & Wang, Y. M. 2004, ApJ, 616, 1224
Sonnerup, B. U. Ö 1979, Space Plasma Physics: The Study of Solar-system Plasmas, Vol. 2 (Amsterdam: North-Holland), 879
Uzdensky, D. A., & Kulsrud, R. M. 2006, PhPl, 13, 062305
Vasyliunas, V. M. 1975, RvGSP, 13, 303
Vilmer, N. 2012, RSPTA, 370, 3241
White, S. M., Benz, A. O., Christe, S., et al. 2011, SSRv, 159, 225
Zank, G. P., le Roux, J. A., Webb, G. M., Dosch, A., & Khabarova, O. 2014, ApJ, 797, 28
Zeiler, A., Biskamp, D., Drake, J. F., et al. 2002, JGR, 107, 1230
Zharkova, V. V., Arzner, K., Benz, A. O., et al. 2011, SSRv, 159, 357